PHOTONICS Research

Unconventional Weyl exceptional contours in non-Hermitian photonic continua

Qinghui Yan,[1,2] Qiaolu Chen,[1,2] Li Zhang,[1,2] Rui Xi,[1,2] Hongsheng Chen,[1,2,3] and Yihao Yang[1,2,4]

[1]Interdisciplinary Center for Quantum Information, State Key Laboratory of Modern Optical Instrumentation, ZJU-Hangzhou Global Scientific and Technological Innovation Center, Zhejiang University, Hangzhou 310027, China
[2]International Joint Innovation Center, Key Laboratory of Advanced Micro/Nano Electronic Devices & Smart Systems of Zhejiang, The Electromagnetics Academy at Zhejiang University, Zhejiang University, Haining 314400, China
[3]e-mail: hansomchen@zju.edu.cn
[4]e-mail: yangyihao@zju.edu.cn

Received 29 July 2021; revised 14 September 2021; accepted 14 September 2021; posted 14 September 2021 (Doc. ID 438769); published 16 November 2021

Unconventional Weyl points with topological charges higher than 1 can transform into various complex unconventional Weyl exceptional contours under non-Hermitian perturbations. However, theoretical studies of these exceptional contours have been limited to tight-binding models. Here, we propose to realize unconventional Weyl exceptional contours in photonic continua—non-Hermitian anisotropic chiral plasma, based on *ab initio* calculation by Maxwell's equations. By perturbing in-plane permittivity, an unconventional Weyl point can transform into a quadratic Weyl exceptional ring, a type I Weyl exceptional chain with one chain point, a type II Weyl exceptional chain with two chain points, or other forms. Realistic metamaterials with effective constitutive parameters are proposed to implement these unconventional Weyl exceptional contours. Our work paves a way toward exploration of exotic physics of unconventional Weyl exceptional contours in non-Hermitian topological photonic continua.

https://doi.org/10.1364/PRJ.438769

1. INTRODUCTION

A photonic Weyl point (WP) [1–14] is the linear point crossing of two bands in three-dimensional (3D) momentum space. As the sources or drains of the Berry flux with $C = +1$ (or $C = -1$, where C is the Chern number) topological charges, WPs are characterized by the helicoid surface states and the discontinuous Fermi arcs at surface boundaries of photonic media [1–4,6,7]. Later studies have shown the charge-1 WP belongs to a big family; others include but are not limited to quadratic Weyl points (QWPs, $C = 2$) [8,15–19], spin-1 WPs ($C = 2$) [17,20–22], charge-2 Dirac points ($C = 2$) [17,20–22], triple WPs ($C = 3$) [8,23], and quadruple WPs ($C = 4$) [24,25]. Members with $C > 1$ charges in the family are generally dubbed the unconventional WPs.

The photonic WPs (conventional and unconventional) can be realized in periodic, precisely engineered, artificial structures, such as photonic crystals [5] and optical waveguide arrays [10], or in photonic continua, such as magnetized semiconductors [13] and metamaterials [12]. In comparison to the periodic structures, the electrodynamics of continua is much simpler, which significantly facilitates gaining deeper physical insights into topological photonics. Besides, many interesting phenomena associated with photonic Weyl media have been observed, including chiral zero modes [26], robust surface states [8,9], and topological self-collimations [19].

The recent rapid development of the non-Hermitian topological band theory [27–29] has brought researchers' attentions to the non-Hermitian generalizations of photonic WPs. For example, under non-Hermitian perturbations, a conventional WP can transform into a Weyl exceptional ring (WER), along which the eigenmodes of two degenerate bands coalesce into one, forming a ring of exceptional points [28]. Such WERs are proposed to exist in periodic structures decorated with gain or loss (e.g., non-Hermitian photonic crystals [30] and non-Hermitian waveguide arrays [31]), and non-Hermitian continua (e.g., lossy magnetized plasma) [32,33]. Interestingly, the WER preserves the topological charge as well as the surface-wave Fermi arcs [29,32]. Besides, recent theoretical works have suggested that the unconventional WP, under non-Hermitian perturbations, can transform into various complex one-dimensional closed exceptional contours, with the topological charges preserved [29]. Several tight-binding models have been proposed to implement those unconventional exceptional contours [29,34]. However, in realistic photonic media, such as photonic crystals and metamaterials, the modes are usually not tightly bound to any site; the band structures of photonic crystals have multiple Bragg scattering in most cases [35].

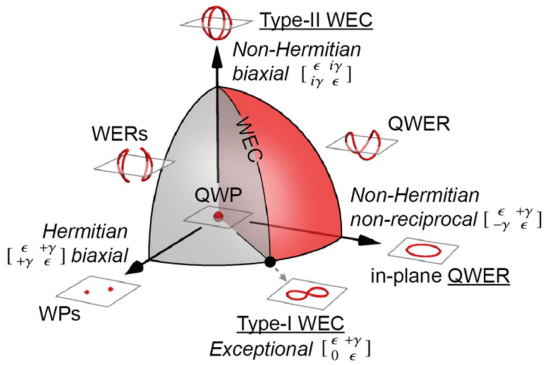

Fig. 1. Unconventional Weyl exceptional contours in non-Hermitian anisotropic chiral plasma, parameterized by the in-plane permittivity. When the contour splits or not, the space is divided into the red part, the gray part, and the boundary in between, corresponding to the QWERs, two separated WERs, and the WECs. Underlined are three special cases that pinned in planes by pseudo-PT symmetries: in-plane QWERs, type I WECs with a single chain point, and type II WECs with two chain points.

Therefore, it is important to establish a framework to study the unconventional Weyl exceptional contours beyond the tight-binding models, especially in the context of photonics.

Here, we study various unconventional Weyl exceptional contours in photonic continua—non-Hermitian chiral plasma, based on the first-principle Maxwell's equations. Interestingly, by considering various perturbations to the in-plane permittivity, including non-Hermitian biaxial perturbations, Hermitian biaxial perturbations, and non-Hermitian non-reciprocal perturbations, we obtain a 3D mapping to sketch all the Hermitian/non-Hermitian generalizations of an unconventional WP and, more specifically, a QWP. As shown in Fig. 1, we systematically identify various forms of unconventional Weyl exceptional contours, including the quadratic Weyl exceptional rings (QWERs), two separated WERs, and the Weyl exceptional chains (WECs), denoted by the red and grey regions and the critical boundary in between, respectively. Among them, we focus on three special cases that are pinned in certain planes by the pseudo-parity-time (pseudo-PT) symmetry, which are in-plane QWERs, type I WECs with one chain point, and type II WECs with two chain points, respectively, as underlined in Fig. 1. To implement the above three cases, we then propose realistic metamaterials with effective constitutive parameters.

2. QUADRATIC WEYL POINT IN HERMITIAN ANISOTROPIC CHIRAL PLASMA

To realize unconventional Weyl exceptional contours, we start by constructing a QWP, which is at the origin of the 3D parameter space (see Fig. 1). We consider a piece of plasma continua with the in-plane (in the *xOy* plane) conductivity described by the lossless Drude model $\sigma = i\omega_p^2/\omega$ (ω_p is the plasma frequency) and consider chirality [36] to break all mirror symmetries [37]. Then, using the auxiliary field method [38–40], we have

$$\begin{bmatrix} & i\nabla\times & -i\mathbf{g} \\ -i\nabla\times & & \\ i\mathbf{g}^T & & \end{bmatrix}\begin{bmatrix}\mathbf{E}\\ \mathbf{H}\\ \mathbf{J}\end{bmatrix} = \omega\begin{bmatrix}\varepsilon & +i\chi & \\ -i\chi & \mu & \\ & & \omega_p^{-2}\end{bmatrix}\begin{bmatrix}\mathbf{E}\\ \mathbf{H}\\ \mathbf{J}\end{bmatrix}, \tag{1}$$

where ε, μ, and χ are permittivity, permeability, and chirality tensors, respectively. **E**, **H**, and **J** are electric field, magnetic field, and current density, respectively. **g** is a matrix denoting in-plane conductivity, i.e., $\mathbf{g} = [1, 0; 0, 1; 0, 0]$.

From Eq. (1) we can qualitatively calculate the photonic bands of the continua. Without losing the generality, we set $\varepsilon = \mu = \omega_p = 1$ and $\chi = -0.4$, and $\nabla \sim i\mathbf{k}$ for the continua. As a result in Fig. 2(a), a QWP exists at the $k = 0$ point at the modified plasma frequency $\omega_p' = \omega_p/(1-\chi^2)^{0.5}$. As it named, the in-plane dispersion is quadratic, indicating that the photon is effectively massive due to the sufficient light–matter interaction with the electronic gas. The calculation of topological charge also proves the QWP: we enclose the $k = 0$ point by a small sphere in momentum space and calculate Wilson loops for different polar angles of the sphere. As shown in Fig. 2(b), as the angle varies from 0 to π, the accumulated phase is $+4\pi$ for the upper band of the point degeneracy (in red), indicating $C = +2$ for $\chi < 0$ (or $C = -2$ for $\chi > 0$), which is consistent with our understanding of the QWP.

3. UNCONVENTIONAL WEYL EXCEPTIONAL CONTOURS IN NON-HERMITIAN ANISOTROPIC CHIRAL PLASMA

With the Hermitian QWP on hand, we still need a strategy to break the hermiticity for the Weyl exceptional contours. Motivated by Ref. [41], we use the perturbative method to expand the band structure of QWP in the local momentum space and see the variation of eigenfrequencies with the constitutive parameters. We rewrite Eq. (1) as

$$-(\mathbf{k}\times + i\chi\omega)\mu^{-1}(\mathbf{k}\times + i\chi\omega)\mathbf{E} + \omega_p^2\mathbf{g}\mathbf{g}^T\mathbf{E} = \omega^2\varepsilon\mathbf{E}, \tag{2}$$

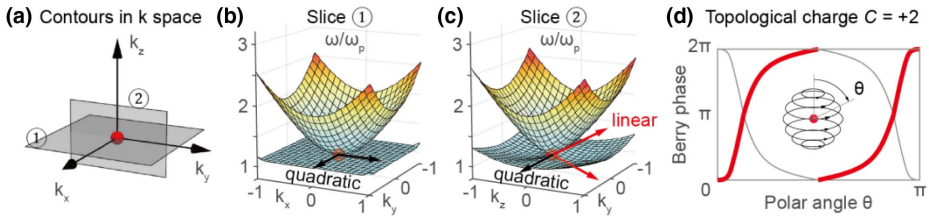

Fig. 2. Quadratic Weyl point in Hermitian anisotropic chiral plasma. (a) Isofrequency contour at the plasma frequency in the k space, where QWP is at the $k = 0$ point. (b) Quadratic in-plane dispersion. (c) Linear out-of-plane dispersion. (d) As $\chi < 0$, the accumulated Berry phase of the circle over the sphere that encloses QWP is $+4\pi$ for the upper band (in red), indicating $C = +2$.

and set $\mu = 1$ for simplicity. Due to the in-plane longitudinality of the wave functions at the QWP ($E_z = 0$), we neglect this component in Eq. (2). By perturbing both the wave vector and the permittivity tensor, the local Hamiltonian around the plasma frequency is (see more detail in Appendix A)

$$H = H_{\mathrm{QWP}} - \delta\varepsilon_{\parallel}, \tag{3}$$

where $\delta\varepsilon_{\parallel}$ is the (zeroth-order) perturbation of the in-plane permittivity under Cartesian coordinates, and H_{QWP} is the local Hamiltonian of the QWP, i.e.,

$$H_{\mathrm{QWP}} = (k_y^2 - k_x^2)\sigma_3 - 2k_x k_y \sigma_1 - \mathrm{sgn}(\chi) k_z \sigma_2, \tag{4}$$

where σ_n, $n = 1, 2, 3$ are the Pauli matrices, and $\mathrm{sgn}(\chi)$ gives the sign of chirality.

Equation (3) bridges the local Hamiltonian and the constitutive parameters of the continua; by tuning the in-plane permittivity, we perturb the local Hamiltonian to turn the QWP into various quadratic Weyl exceptional contours. The perturbation term can be decomposed by the four Pauli matrices with complex coefficients, denoted as $\gamma_n\sigma_n$, where $n = 0, 1, 2, 3$, and γ_n is complex. Therefore, there are eight degrees of freedom in total, which we are going to discuss in the following text.

A. Hermitian Perturbations to the In-Plane Permittivity

To analyze the Hermitian perturbations to the QWP, we refer to the idea of topological photonics, which treats QWP as the superposition of two WPs pinned by the rotational symmetry [23,42]. Since the WP is robust against any Hermitian perturbation, there are no other ways of evolution than to split the QWP into two WPs. More specifically, the $\gamma\sigma_0$ term (γ is a positive real number) performs a trivial perturbation that simply changes the frequency of QWP. The $\gamma\sigma_2$ term shifts the QWP along the k_z direction, corresponding to the gyrotropic material with a magnetic axis in the z direction that breaks the time-reversal (T) symmetry. This partially explains why the QWP at the Γ point is missing in previous works on magnetized plasmas [32,33]. As for the $\gamma\sigma_1$ term (or $\gamma\sigma_3$ term, which is equivalent by $\pi/4$ rotation along the z axis), which is a biaxial anisotropic one that breaks the continuous rotational symmetry along the z direction ($C_{\infty z}$) down to twofold rotational symmetry C_{2z}, the QWP splits into two in-plane WPs as shown in Fig. 3(a).

B. Non-Hermitian Perturbations to the In-Plane Permittivity

It has been known that the WER is the non-Hermitian generalization of a WP [28], the QWP is the superposition of two identical WPs [23], and multiple WERs can touch and emerge into one WER [29]. In the following, we will show that the non-Hermitian generalization of a QWP can be a single exceptional ring or two exceptional rings with various connections.

We start the analysis with the $i\gamma\sigma_0$ term that corresponds to the addition of an isotropic lossy term onto the permittivity. The lossy term keeps the degeneracy of the QWP, even though the eigenfrequency is complex. This can be understood from the lossy Drude model, which does not lead to exceptional contours at the plasma frequency.

For the $i\gamma\sigma_2$ term, as shown in Fig. 3(b), the two WPs inside the QWP expand into two identical WERs to form a QWER.

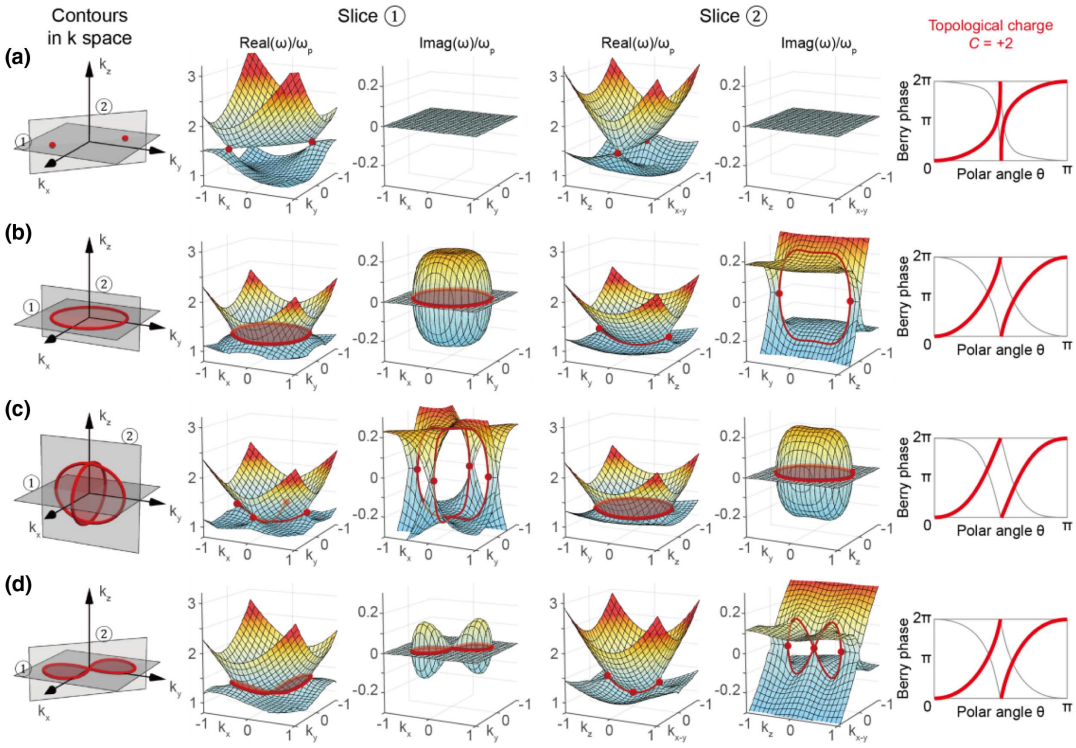

Fig. 3. Four typical cases evolving from the QWP. (a) Two WPs, where $\varepsilon_{\parallel} = [1, 0.4; 0.4, 1]$. (b) QWER, where $\varepsilon_{\parallel} = [1, 0.4; -0.4, 1]$. (c) Type II WEC, where $\varepsilon_{\parallel} = [1, 0.4i; 0.4i, 1]$. (d) Type I WEC, where $\varepsilon_{\parallel} = [1, 0.4; 0, 1]$. For each case we plot the exceptional contour, the band diagrams in the slices indicated in the left panel, and the Wilson loop on a sphere covering the unconventional Weyl exceptional contours.

Moreover, we find the $C_{2z}T$ symmetry acts as a pseudo-PT symmetry in the $k_z = 0$ plane. Given a mode labelled with (k_x, k_y, k_z, ω), the C_{2z} symmetry maps the mode into another mode labeled with $(-k_x, -k_y, k_z, \omega)$, while the T symmetry into $(-k_x^*, -k_y^*, -k_z^*, \omega^*)$. Thus, at the $k_z = 0$ plane, $C_{2z}T$ together maps $(k_x, k_y, 0, \omega)$ to $(k_x, k_y, 0, \omega^*)$, which is identical to the PT symmetry (we thus refer to it as the pseudo-PT symmetry hereafter). Therefore, modes in the in-plane part of the band are either in an exact-pseudo-PT phase where eigenfrequencies are all real numbers, or in a broken-pseudo-PT phase where bands are coupled in pairs with conjugate eigenfrequencies; the QWER lies at the boundary between two phases. As shown in Fig. 3(b), the red circle is the exceptional ring, and the red area is of broken-pseudo-PT phase.

For the $i\gamma\sigma_1$ term (or the $i\gamma\sigma_3$ term), as shown in Fig. 3(c), the QWP transforms into two orthogonal WERs, which cross with each other at two points along the k_z axis. We thus refer to it as the type II WEC. T symmetry no longer exists for this material; instead are the $C_{2x}T$ and the $C_{2y}T$ symmetries acting as pseudo-PT symmetries that pin the two WERs in the $k_x = 0$ plane and the $k_y = 0$ plane, respectively. Moreover, two WERs are related by $C_{4z}T$, so we only plot one of them in Fig. 3(c).

C. Unconventional Weyl Exceptional Contours in the In-Plane Permittivity Parameter Space

Above, we have discussed all eight types of perturbations. Only three of them lead to nontrivial deformations, i.e., Real(γ_1), Imag(γ_2), and Imag(γ_1), where Real(·) and Imag(·) give the real and imaginary parts of the input, respectively, as shown in Table 1. The rest of the perturbations merely shift, rotate, or tilt the contour that does not change the connection. Therefore, we can study the unconventional Weyl exceptional contours in a 3D parameter space corresponding to the in-plane permittivity tensor. Recalling Fig. 1, besides the exceptional contours along the three axes and the original point, we calculate the exceptional contours for the remaining part of the space and pick out three intermediate states between every two axes to depict how the exceptional contour evolves as the in-plane permittivity varies. Depending on whether the QWER splits into two WERs or not [Real(γ_1) − Imag(γ_2) > 0 or <0], the space can be divided into two regions (gray and red). At the critical boundary [Real(γ_1) − Imag(γ_2) = 0], two WERs are critically connected to form the WEC.

Besides the type II WEC, we find another interesting case on the boundary, namely, the type I WEC, where the two WERs are in the same plane (pinned by $C_{2z}T$) with only one chain point at the $k = 0$ point (pinned by C_{2z}) as shown in Fig. 3(d) and the fifth column in Table 1. Due to the same strength of perturbation by σ_1 and $i\sigma_2$, the perturbation term is upper-triangular, which is the sign of exceptional structures. Consequently, the in-plane permittivity is exceptional with coalesced eigenmodes at the chain point at the $k = 0$ point. In a broader sense, the chain point is pinned at the $k = 0$ point if and only if

$$\gamma_1^2 + \gamma_2^2 + \gamma_3^2 = 0, \tag{5}$$

where $\gamma_{1,2,3}$ are complex numbers that should not be zero simultaneously, otherwise, the perturbation term vanishes.

4. METAMATERIAL DESIGN TO ACHIEVE THE UNCONVENTIONAL WEYL EXCEPTIONAL CONTOURS

In the following, we design a metamaterial structure to implement the QWP, and then we add perturbations to the background permittivity to achieve the unconventional Weyl exceptional contours. As shown in Fig. 4(a), the unit cell is cuboid with periods $p_x = p_y = 7$ mm, $p_z = 10$ mm along the x, y, and z directions, respectively. In each unit cell, there is a metallic resonant structure made with 0.7 mm thickness rods. The structure can be considered as the deformation of two in-plane split-ring resonators, described by the Drude–Lorentz model with a resonant frequency at about 6.3 GHz. Besides, the slits of the split-ring resonators are offset from the center point of the skeleton. In doing so, all mirror symmetries are broken, and the chirality is introduced. Here, the structural parameters are $d = 0.7$ mm, $h_x = h_y = 6.0$ mm, $h_z = 2.9$ mm, and offset = 1.0 mm. The spatial group of the unit cell is No. 89 ($P422$). Suppose the background material has $\varepsilon = 4$ and $\mu = 1$, and then at the Γ point ($k = 0$), the third and the fourth bands intersect as a QWP. Note that the QWP has been experimentally realized at microwave [19] and infrared frequencies [15].

Then, by tuning the in-plane permittivity of the background material, different exceptional contours emerge as predicted. As shown in Fig. 4(b), $\varepsilon_{xx} = \varepsilon_{yy} = 4$ and $\varepsilon_{xy} = -\varepsilon_{yx} = 0.5$, i.e., the $i\gamma_2\sigma_2$ type, and thus the QWP expands into a QWER. Due to the C_4 symmetry, the contour is not a perfect circle. By breaking the C_{2x} and C_{2y} symmetries, the magnetic spatial group falls down to No. 75.2 ($P41'$).

Table 1. Variants of QWP When Introducing Perturbations to the In-Plane Permittivity, Where ε and γ are Real Numbers[a]

Contours	Two WPs	In-plane QWER	Type II WEC	Type I WEC
Figures	Fig. 3(a)	Fig. 3(b)	Fig. 3(c)	Fig. 3(d)
Perturbations	$\gamma\sigma_1$	$i\gamma\sigma_2$	$i\gamma\sigma_1$	$\gamma(\sigma_1 + i\sigma_2)$
$\varepsilon_{\parallel}$	$\begin{bmatrix} \varepsilon & +\gamma \\ +\gamma & \varepsilon \end{bmatrix}$ Hermitian biaxial	$\begin{bmatrix} \varepsilon & +\gamma \\ -\gamma & \varepsilon \end{bmatrix}$ Non-Hermitian nonreciprocal	$\begin{bmatrix} \varepsilon & +i\gamma \\ +i\gamma & \varepsilon \end{bmatrix}$ Non-Hermitian biaxial	$\begin{bmatrix} \varepsilon & +2\gamma \\ 0 & \varepsilon \end{bmatrix}$ Non-Hermitian exceptional
Symmetries	T, C_{2z}, $C_{2z}T$	T, $C_{\infty z}$, $\underline{C_{2z}T}$	$C_{4z}T$, $\underline{C_{2x}T}$, $\underline{C_{2y}T}$	T, C_{2z}, $\underline{C_{2z}T}$

[a]Underlined are the pseudo-PT operators that respectively pin the exceptional contours in one of the $k_\alpha = 0$ planes, where $\alpha = x, y, z$.

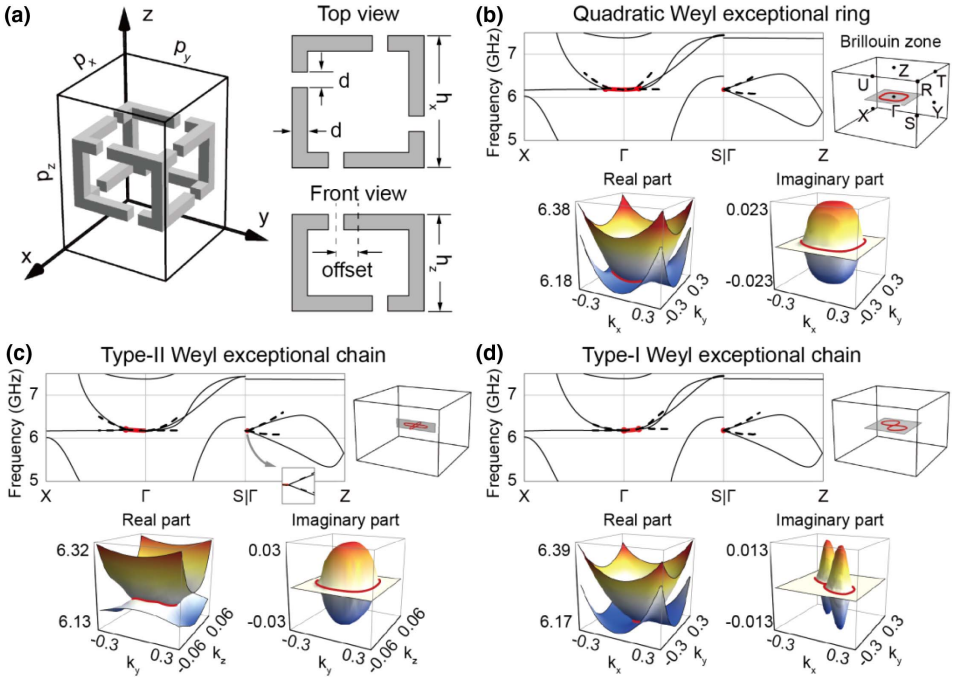

Fig. 4. Metamaterial designs to implement various unconventional Weyl exceptional contours. (a) Unit cell of metamaterial. The metallic structure (in gray) is designed to create in-plane resonance to introduce chirality. By switching the in-plane permittivity of the background material to $[4.0, 0.5; -0.5, 4.0]$, $[4.0, 0.5i; 0.5i, 4.0]$, and $[4.0, 0.5; -0.06, 4.0]$, respectively, the third and the fourth bands intersect as (b) the QWER, (c) the type II WEC, and (d) the type I WEC around 6.3 GHz in the vicinity of the Γ point, respectively. All exceptional contours are pinned inside one of the $k_\alpha = 0$ planes by $C_{2\alpha}T$ symmetries, where $\alpha = x, y, z$. The gray area in the Brillouin zone in (b)–(d) covers the exceptional contour, where a detailed band plot is given to show the real and imaginary parts of the eigenfrequencies. k_x and k_y are normalized by π/p_x and π/p_y, respectively. For each case in (b)–(d), we fit the bulk bands by the continua model with effective constitutive parameters, plotted in dashed black curves in the vicinity of the Γ point. Note that in (d), in-plane permittivity is not rigorously upper-triangular due to the nonlocal effect.

As shown in Fig. 4(c), if we apply $\varepsilon_{xy} = \varepsilon_{yx} = 0.5i$ to the background media, i.e., the $i\gamma_1\sigma_1$ type, the QWP turns into a type II WEC. Due to the strong anisotropy, the chain is greatly pressed along the z direction. The magnetic spatial group is No. 89.91 ($P4'2'2$).

As shown in Fig. 4(d), as $\varepsilon_{xy} = 0.5$ and $\varepsilon_{yx} \approx -0.06$, the QWP turns into a type I WEC that is pinned by the $C_{2z}T$ symmetry with chain point at the $k = 0$ point. The in-plane permittivity is slightly biased from upper-triangular, because k is comparable to $2\pi/p_x$ or $2\pi/p_y$ (the length of the Brillouin zone), and the nonlocal effect more or less induces higher-order dispersions that twist the photonic bands. The effect is negligible as the size of the Brillouin zone is finite. The magnetic spatial group is No. 3.2 ($P21'$).

Then, we fit the bulk bands of the metamaterials by the continua model. As shown in Figs. 4(b)–4(d), in the vicinity of the exceptional contours, we plot the fitting results by dashed curves, with constitutive parameters $\varepsilon = 4$ and $\omega_p = 2\pi \times 12.2$ GHz. Due to the magnetic resonance of the split-ring resonator, the permeability is greater than 1, i.e., $\mu_{xx} = \mu_{yy} = 4$, $\mu_{zz} = 7$. The chirality is $\chi = 0.7$. One can observe that different perturbations lead to different off-diagonal elements of the effective permittivity tensor. Here, we have $\varepsilon_{xy} = -\varepsilon_{yx} = -0.05$ for the QWER, $\varepsilon_{xy} = \varepsilon_{yx} = 0.04i$ for the type II WEC, and $\varepsilon_{yx} = -0.07$ for the type I WEC.

At last, we note that all variants of QWP preserve the $C = +2$ topological charge as verified by our first-principles calculations as shown in Appendix B.

5. DISCUSSION

We have thus theoretically identified various unconventional Weyl exceptional contours in the non-Hermitian photonic continua, including the QWER, the type I WEC with one chain point, and the type II WEC with two chain points. Based on the Maxwell's equations and the perturbative method, we bridge the local Hamiltonian of unconventional Weyl exceptional contours with the constitutive parameters of the non-Hermitian photonic continua. Several metamaterials with effective constitutive parameters have been designed to implement the unconventional Weyl exceptional contours. Besides, it would be interesting to investigate the directional amplification based on the QWER with broken hermiticity and reciprocity while preserving the T symmetry [43], and the arbitrary gain/loss control of light polarization based on the WEC with complex symmetric anisotropic permittivity [44]. With the recent rapid development in photonic metamaterials 47–45]], it is possible to experimentally implement those unconventional Weyl exceptional contours in the future. The contours as well as the associated double surface Fermi arcs (see Appendix B) should be experimentally observable

[31,48], which can distinguish the quadratic Weyl exceptional contours from their Hermitian counterpart. Finally, our work sheds light on the exploration of exotic physics of unconventional Weyl exceptional contours in non-Hermitian topological photonic continua, such as non-Hermitian skin effect [49].

APPENDIX A: INTUITIVE DERIVATION ON THE LOCAL HAMILTONIAN OF THE QUADRATIC WEYL POINT AND THE PERTURBATION BY THE PERMITTIVITY

The perturbed local Hamiltonian provides a brief formula to estimate the variation of photonic bands caused by the variation of constitutive parameters [41]. In our case, the local Hamiltonian is an operator whose eigenvalues are the small variations of angular frequencies in the vicinity of ω_p' at the $k=0$ point. To derive the local Hamiltonian of the quadratic Weyl point, we first write down Maxwell's equations with the auxiliary field

$$\begin{bmatrix} & +i\nabla\times & -i\omega_p\mathbf{g} \\ -i\nabla\times & & \\ +i\omega_p\mathbf{g}^T & & \end{bmatrix}\begin{bmatrix}\mathbf{E}\\ \mathbf{H}\\ \mathbf{J}\end{bmatrix} = \omega\begin{bmatrix}\varepsilon & +i\chi & \\ -i\chi & \mu & \\ & & 1\end{bmatrix}\begin{bmatrix}\mathbf{E}\\ \mathbf{H}\\ \mathbf{J}\end{bmatrix}. \tag{A1}$$

In a homogeneous material, $\nabla\sim i\mathbf{k}$. Suppose $\varepsilon_0=\mu_0=1$ and $\mu=1$, and move the chirality term to the left side:

$$\begin{bmatrix} & -\mathbf{k}\times -i\chi\omega & -i\omega_p\mathbf{g} \\ +\mathbf{k}\times +i\chi\omega & & \\ +i\omega_p\mathbf{g}^\dagger & & \end{bmatrix}\begin{bmatrix}\mathbf{E}\\ \mathbf{H}\\ \mathbf{J}\end{bmatrix} = \omega\begin{bmatrix}\varepsilon & & \\ & 1 & \\ & & 1\end{bmatrix}\begin{bmatrix}\mathbf{E}\\ \mathbf{H}\\ \mathbf{J}\end{bmatrix}. \tag{A2}$$

Rewrite Eq. (A2) in the form of $D\psi=\omega M\psi$. Then doubling the operator $M^{-1}D$ for $M^{-1}DM^{-1}D\psi=\omega^2\psi$ to decouple the electric field and the magnetic field. Picking out the electric part, we have

$$-(\mathbf{k}\times +i\chi\omega)^2\mathbf{E}+\omega_p^2\mathbf{g}\mathbf{g}^T\mathbf{E}=\omega^2\varepsilon\mathbf{E}. \tag{A3}$$

As $\varepsilon=1$, it is Eq. (2) in the main text.

If $\varepsilon_\parallel=1$, then at the $k=0$ point around $\omega_p'=\omega_p/(1-\chi^2)^{0.5}$ there is a quadratic Weyl point, whose electric field has no out-of-plane component, so we cancel E_z,

$$\left(k_z^2+\begin{bmatrix}k_y^2 & k_xk_y\\ k_xk_y & k_x^2\end{bmatrix}-2\chi k_z\omega\begin{bmatrix} & -i\\ +i & \end{bmatrix}\right)\mathbf{E}_\parallel = (\omega^2\varepsilon_\parallel-\chi^2\omega^2-\omega_p^2)\mathbf{E}_\parallel, \tag{A4}$$

where the subscript $\parallel$ denotes the field and the tensor with it are in-plane.

To derive the local Hamiltonian, supposing a small variation of angular frequency $\delta\omega$ from ω_p', we have

$$\left(k_z^2+\begin{bmatrix}k_y^2 & k_xk_y\\ k_xk_y & k_x^2\end{bmatrix}-2\chi k_z\omega_p'\begin{bmatrix} & -i\\ +i & \end{bmatrix}\right)\mathbf{E}_\parallel = \left(2(1-\chi^2)\omega_p'\delta\omega+2\chi k_z\delta\omega\begin{bmatrix} & -i\\ +i & \end{bmatrix}\right)\mathbf{E}_\parallel. \tag{A5}$$

In the vicinity of the $k=0$ point, the line-crossed term is small. By neglecting this term and other coefficients that do not affect the topological properties, we have the local Hamiltonian of the quadratic Weyl point

$$\begin{aligned} H_{\mathrm{QWP}} &\sim k_z^2+\begin{bmatrix}k_y^2 & -k_xk_y\\ -k_xk_y & k_x^2\end{bmatrix}-\frac{1}{2}\mathrm{sgn}(\chi)k_z\begin{bmatrix} & -i\\ +i & \end{bmatrix}\\ &= \cancel{\left(k_z^2+\frac{1}{2}k_x^2+\frac{1}{2}k_y^2\right)}\sigma_0+\frac{1}{2}(k_y^2-k_x^2)\sigma_3\\ &\quad -k_xk_y\sigma_1-\frac{1}{2}\mathrm{sgn}(\chi)k_z\sigma_2, \end{aligned} \tag{A6}$$

which is Eq. (4) in the main text.

As the perturbation term is added to the permittivity, the variation of $\omega^2\varepsilon_\parallel$ on the right side of Eq. (A4) is $\delta(\omega^2\varepsilon_\parallel)=2\omega_p'\delta\omega\varepsilon_\parallel+\omega_p'^2\delta\varepsilon_\parallel$, where the line-crossed term is nonzero. Following the same procedure as above and neglecting some coefficients, we have

$$H_{\mathrm{QWP}}\mathbf{E}_\parallel=\delta\omega\mathbf{E}_\parallel+\delta\varepsilon_\parallel\mathbf{E}_\parallel, \tag{A7}$$

which leads to Eq. (3) in the main text.

Our intuitive derivation is equivalent to the rigorous degenerate-state perturbative method by auxiliary field method with Maxwell's equations [50].

APPENDIX B: TOPOLOGICAL CHARGE AND FERMI ARCS OF THE QWP AND ITS VARIANTS IN METAMATERIAL STRUCTURES

In this section, we perform first-principles calculations of the metamaterial model to obtain the topological charges and the Fermi arcs of the QWP and its non-Hermitian variants.

We first calculate the Chern numbers by the Wilson-loop method. In each case, we enclose the QWP or the quadratic

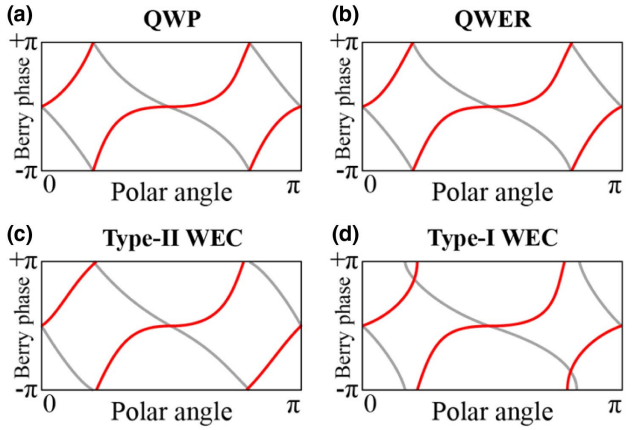

Fig. 5. Evolution of Berry phases on the latitude circles of the spheres enclosing (a) QWP, (b) QWER, (c) type II WEC, and (d) type I WEC. As the polar angle varies from 0 to π, the accumulated phases imply the topological charge $C=+2$.

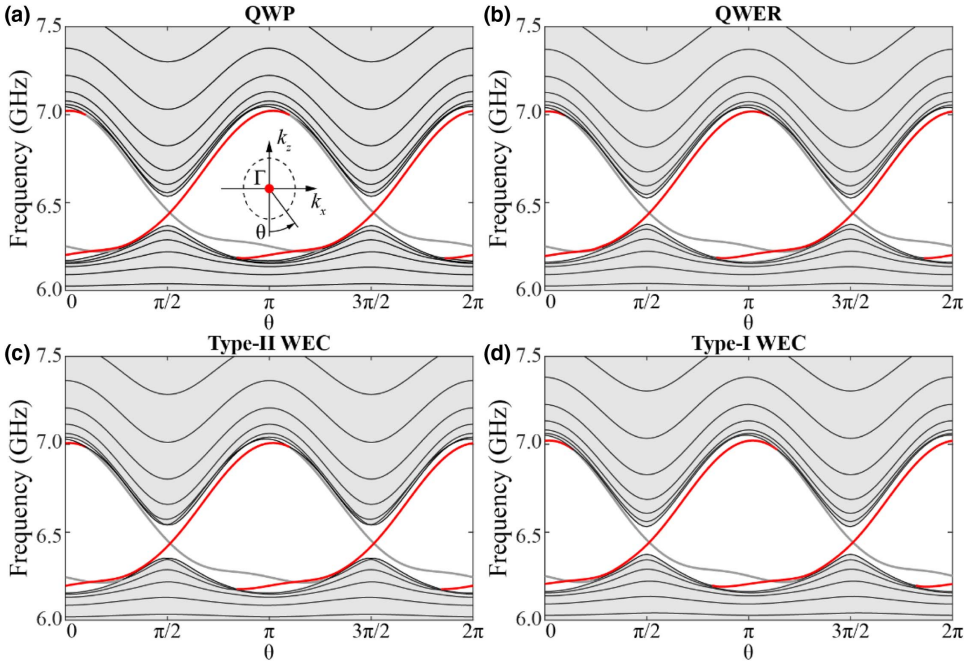

Fig. 6. k_y-projected surface band structure along an ellipse enclosing the Γ point. (a) QWP, (b) QWER, (c) type II WEC, and (d) type I WEC. The red lines denote the Fermi arc surface states.

Weyl exceptional contours by a sphere and calculate the Berry phases on different latitude circles. As the polar angle ranges from 0 to π, the evolutions of Berry phases are shown in Fig. 5. The accumulated Berry phases are $+4\pi$ for all four cases, indicating the topological charge $C = +2$.

Next, we calculate the surface Fermi arcs emanating from the QWP and its variants. We note that the QWP in Fig. 4 is overlapped with the other trivial bands when projected to a plane, leading to the difficulty to observe surface Fermi arcs. Alternatively, we choose another structure proposed by us in Ref. [19], which also features a QWP with $C = +2$ at the Γ point. Based on the model in Ref. [19], we obtain the projected surface band structure along a closed curve enclosing the Γ point as shown in Fig. 6. The two red lines in each panel indicate the two surface Fermi arcs emanating from either the QWP or its non-Hermitian variants.

Funding. Top-Notch Young Talents Program of China; Fundamental Research Funds for the Central Universities; National Natural Science Foundation of China (11961141010, 61625502, 61975176, U19A2054).

Disclosures. The authors declare no conflicts of interest.

Data Availability. Data underlying the results presented in this paper are not publicly available at this time but may be obtained from the authors upon reasonable request.

REFERENCES

1. X. Wan, A. M. Turner, A. Vishwanath, and S. Y. Savrasov, "Topological semimetal and Fermi-arc surface states in the electronic structure of pyrochlore iridates," Phys. Rev. B **83**, 205101 (2011).
2. B. Q. Lv, H. M. Weng, B. B. Fu, X. P. Wang, H. Miao, J. Ma, P. Richard, X. C. Huang, L. X. Zhao, G. F. Chen, Z. Fang, X. Dai, T. Qian, and H. Ding, "Experimental discovery of Weyl semimetal TaAs," Phys. Rev. X **5**, 031013 (2015).
3. N. P. Armitage, E. J. Mele, and A. Vishwanath, "Weyl and Dirac semimetals in three-dimensional solids," Rev. Mod. Phys. **90**, 015001 (2018).
4. L. Lu, L. Fu, J. D. Joannopoulos, and M. Soljačić, "Weyl points and line nodes in gyroid photonic crystals," Nat. Photonics **7**, 294–299 (2013).
5. L. Lu, Z. Wang, D. Ye, L. Ran, L. Fu, J. D. Joannopoulos, and M. Soljacic, "Experimental observation of Weyl points," Science **349**, 622–624 (2015).
6. M. Xiao, W.-J. Chen, W.-Y. He, and C. T. Chan, "Synthetic gauge flux and Weyl points in acoustic systems," Nat. Phys. **11**, 920–924 (2015).
7. S.-Y. Xu, I. Belopolski, N. Alidoust, M. Neupane, G. Bian, C. Zhang, R. Sankar, G. Chang, Z. Yuan, C.-C. Lee, S.-M. Huang, H. Zheng, J. Ma, D. S. Sanchez, B. Wang, A. Bansil, F. Chou, P. P. Shibayev, H. Lin, S. Jia, and M. Z. Hasan, "Discovery of a Weyl fermion semimetal and topological Fermi arcs," Science **349**, 613–617 (2015).
8. W.-J. Chen, M. Xiao, and C. T. Chan, "Photonic crystals possessing multiple Weyl points and the experimental observation of robust surface states," Nat. Commun. **7**, 13038 (2016).
9. B. Yang, Q. Guo, B. Tremain, L. E. Barr, W. Gao, H. Liu, B. Béri, Y. Xiang, D. Fan, A. P. Hibbins, and S. Zhang, "Direct observation of topological surface-state arcs in photonic metamaterials," Nat. Commun. **8**, 97 (2017).
10. J. Noh, S. Huang, D. Leykam, Y. D. Chong, K. P. Chen, and M. C. Rechtsman, "Experimental observation of optical Weyl points and Fermi arc-like surface states," Nat. Phys. **13**, 611–617 (2017).
11. M. Zhou, L. Ying, L. Lu, L. Shi, J. Zi, and Z. Yu, "Electromagnetic scattering laws in Weyl systems," Nat. Commun. **8**, 1 (2017).
12. B. Yang, Q. Guo, B. Tremain, R. Liu, L. E. Barr, Q. Yan, W. Gao, H. Liu, Y. Xiang, J. Chen, C. Fang, A. Hibbins, L. Lu, and S. Zhang, "Ideal Weyl points and helicoid surface states in artificial photonic crystal structures," Science **359**, 1013–1016 (2018).
13. D. Wang, B. Yang, W. Gao, H. Jia, Q. Yang, X. Chen, M. Wei, C. Liu, M. Navarro, J. Han, W. Zhang, and S. Zhang, "Photonic Weyl points due to broken time-reversal symmetry in magnetized semiconductor," Nat. Phys. **15**, 1150–1155 (2019).

14. W. Gao, B. Yang, M. Lawrence, F. Fang, B. Béri, and S. Zhang, "Photonic Weyl degeneracies in magnetized plasma," Nat. Commun. **7**, 12435 (2016).
15. S. Vaidya, J. Noh, A. Cerjan, C. Jörg, G. von Freymann, and M. C. Rechtsman, "Observation of a charge-2 photonic Weyl point in the infrared," Phys. Rev. Lett. **125**, 253902 (2020).
16. S.-M. Huang, S.-Y. Xu, I. Belopolski, C.-C. Lee, G. Chang, T.-R. Chang, B. Wang, N. Alidoust, G. Bian, M. Neupane, D. Sanchez, H. Zheng, H.-T. Jeng, A. Bansil, T. Neupert, H. Lin, and M. Z. Hasan, "New type of Weyl semimetal with quadratic double Weyl fermions," Proc. Natl. Acad. Sci. USA **113**, 1180–1185 (2016).
17. T. Zhang, Z. Song, A. Alexandradinata, H. Weng, C. Fang, L. Lu, and Z. Fang, "Double-Weyl phonons in transition-metal monosilicides," Phys. Rev. Lett. **120**, 016401 (2018).
18. H. He, C. Qiu, X. Cai, M. Xiao, M. Ke, F. Zhang, and Z. Liu, "Observation of quadratic Weyl points and double-helicoid arcs," Nat. Commun. **11**, 1820 (2020).
19. Y. Yang, Z. Gao, X. Feng, Y.-X. Huang, P. Zhou, S. A. Yang, Y. Chong, and B. Zhang, "Ideal unconventional Weyl point in a chiral photonic metamaterial," Phys. Rev. Lett. **125**, 143001 (2020).
20. D. S. Sanchez, I. Belopolski, T. A. Cochran, X. Xu, J.-X. Yin, G. Chang, W. Xie, K. Manna, V. Süß, C.-Y. Huang, N. Alidoust, D. Multer, S. S. Zhang, N. Shumiya, X. Wang, G.-Q. Wang, T.-R. Chang, C. Felser, S.-Y. Xu, S. Jia, H. Lin, and M. Z. Hasan, "Topological chiral crystals with helicoid-arc quantum states," Nature **567**, 500–505 (2019).
21. Z. Rao, H. Li, T. Zhang, S. Tian, C. Li, B. Fu, C. Tang, L. Wang, Z. Li, W. Fan, J. Li, Y. Huang, Z. Liu, Y. Long, C. Fang, H. Weng, Y. Shi, H. Lei, Y. Sun, T. Qian, and H. Ding, "Observation of unconventional chiral fermions with long Fermi arcs in CoSi," Nature **567**, 496–499 (2019).
22. Y. Yang, H. Sun, J. Xia, H. Xue, Z. Gao, Y. Ge, D. Jia, S. Yuan, Y. Chong, and B. Zhang, "Topological triply degenerate point with double Fermi arcs," Nat. Phys. **15**, 645–649 (2019).
23. C. Fang, M. J. Gilbert, X. Dai, and B. A. Bernevig, "Multi-Weyl topological semimetals stabilized by point group symmetry," Phys. Rev. Lett. **108**, 266802 (2012).
24. T. Zhang, R. Takahashi, C. Fang, and S. Murakami, "Twofold quadruple Weyl nodes in chiral cubic crystals," Phys. Rev. B **102**, 125148 (2020).
25. C. Cui, X.-P. Li, D.-S. Ma, Z.-M. Yu, and Y. Yao, "Charge-4 Weyl point: minimum lattice model and chirality-dependent properties," Phys. Rev. B **104**, 075115 (2021).
26. H. Jia, R. Zhang, W. Gao, Q. Guo, B. Yang, J. Hu, Y. Bi, Y. Xiang, C. Liu, and S. Zhang, "Observation of chiral zero mode in inhomogeneous three-dimensional Weyl metamaterials," Science **363**, 148–151 (2019).
27. H. Shen, B. Zhen, and L. Fu, "Topological band theory for non-Hermitian Hamiltonians," Phys. Rev. Lett. **120**, 146402 (2018).
28. Y. Xu, S.-T. Wang, and L.-M. Duan, "Weyl exceptional rings in a three-dimensional dissipative cold atomic gas," Phys. Rev. Lett. **118**, 045701 (2017).
29. A. Cerjan, M. Xiao, L. Yuan, and S. Fan, "Effects of non-Hermitian perturbations on Weyl Hamiltonians with arbitrary topological charges," Phys. Rev. B **97**, 075128 (2018).
30. H. Zhou, J. Y. Lee, S. Liu, and B. Zhen, "Exceptional surfaces in PT-symmetric non-Hermitian photonic systems," Optica **6**, 190–193 (2019).
31. A. Cerjan, S. Huang, M. Wang, K. P. Chen, Y. Chong, and M. C. Rechtsman, "Experimental realization of a Weyl exceptional ring," Nat. Photonics **13**, 623–628 (2019).
32. W. Wang, W. Gao, L. Cao, Y. Xiang, and S. Zhang, "Photonic topological Fermi nodal disk in non-Hermitian magnetic plasma," Light Sci. Appl. **9**, 1 (2020).
33. K. Shastri and F. Monticone, "Dissipation-induced topological transitions in continuous Weyl materials," Phys. Rev. Res. **2**, 033065 (2020).
34. D. Chowdhury, A. Banerjee, and A. Narayan, "Light-driven Lifshitz transitions in non-Hermitian multi-Weyl semimetals," Phys. Rev. A **103**, L051101 (2021).
35. J. D. Joannopoulos, S. G. Johnson, J. N. Winn, and R. D. Meade, *Molding the Flow of Light* (Princeton University, 2008), p. 44.
36. Y. Cheng, W. Li, and X. Mao, "Triple-band polarization angle independent 90° polarization rotator based on Fermat's spiral structure planar chiral metamaterial," Prog. Electromagn. Res. **165**, 35–45 (2019).
37. J. D. Joannopoulos, S. G. Johnson, J. N. Winn, and R. D. Meade, *Molding the Flow of Light* (Princeton University, 2008), p. 37.
38. A. Raman and S. Fan, "Photonic band structure of dispersive metamaterials formulated as a Hermitian eigenvalue problem," Phys. Rev. Lett. **104**, 087401 (2010).
39. F. Binkowski, L. Zschiedrich, and S. Burger, "An auxiliary field approach for computing optical resonances in dispersive media," J. Eur. Opt. Soc. Publ. **15**, 1 (2019).
40. M. G. Silveirinha, "Chern invariants for continuous media," Phys. Rev. B **92**, 125153 (2015).
41. J. D. Joannopoulos, S. G. Johnson, J. N. Winn, and R. D. Meade, *Molding the Flow of Light* (Princeton University, 2008), p. 18.
42. Z.-M. Yu, Z. Zhang, G.-B. Liu, W. Wu, X.-P. Li, R.-W. Zhang, S. A. Yang, and Y. Yao, "Encyclopedia of emergent particles in three-dimensional crystals," arXiv:2102.01517v2 (2021).
43. S. Buddhiraju, A. Song, G. T. Papadakis, and S. Fan, "Nonreciprocal metamaterial obeying time-reversal symmetry," Phys. Rev. Lett. **124**, 257403 (2020).
44. A. Cerjan and S. Fan, "Achieving arbitrary control over pairs of polarization states using complex birefringent metamaterials," Phys. Rev. Lett. **118**, 253902 (2017).
45. C. Wang, C. Qian, H. Hu, L. Shen, Z. J. Wang, H. Wang, Z. Xu, B. Zhang, H. Chen, and X. Lin, "Superscattering of light in refractive-index near-zero environments," Prog. Electromagn. Res. **168**, 15–23 (2020).
46. P. Xie, G.-M. Wang, H.-P. Li, Y.-W. Wang, and B. Zong, "Wideband RCS reduction of high gain Fabry-Perot antenna employing a receiver-transmitter metasurface," Prog. Electromagn. Res. **169**, 103–115 (2020).
47. C. L. Holloway, E. F. Kuester, and A. H. Haddab, "Retrieval approach for determining surface susceptibilities and surface porosities of a symmetric metascreen from reflection and transmission coefficients," Prog. Electromagn. Res. **166**, 1–22 (2019).
48. B. Zhen, C. W. Hsu, Y. Igarashi, L. Lu, I. Kaminer, A. Pick, S.-L. Chua, J. D. Joannopoulos, and M. Soljačić, "Spawning rings of exceptional points out of Dirac cones," Nature **525**, 354–358 (2015).
49. K. Zhang, Z. Yang, and C. Fang, "Universal non-Hermitian skin effect in two and higher dimensions," arXiv:2102.05059v2 (2021).
50. A. Raman and S. Fan, "Perturbation theory for plasmonic modulation and sensing," Phys. Rev. B **83**, 205131 (2011).